



**POLITECNICO  
MILANO 1863**

School of Industrial and Information Engineering  
Department of Aerospace Science and Technology - DAER  
MSc in Space Engineering

Final Project  
Spacecraft Attitude Dynamics  
Group n. 10 - Project n. 474

# **Modeling and Analysis of a Earth-observation microsat**

Professor: Franco Bernelli Zazzera

10773170 Coppola Riccardo  
10766366 Corbo Nicolò  
11071847 Jönsson Jonathan  
10764398 Spitalieri Martina

BSc Aerospace Engineering (PoliMi)  
BSc Aerospace Engineering (PoliMi)  
BSc Space Engineering (Luleå  
University of Technology)  
BSc Aerospace Engineering (PoliMi)

Delivery date: 07/01/2025

Academic Year 2024/2025

# Abstract

This report aims to illustrate the preliminary model and analysis performed using MATLAB/Simulink<sup>®</sup> of a microsat attitude dynamics and functioning along its orbit. An existing mission similar to the assigned requirements was chosen and the microsat CE-SAT-IE from Canon Electronics Inc. was considered as an example.

The project takes into account the modeling of the real system, i.e. the real dynamics and kinematics of the spacecraft expressed through quaternions, as well as the environmental disturbances acting on it; moreover, regarding the model of the discrete system, in this project the spacecraft is supposed to be equipped with a star sensor and a gyroscope for attitude determination, as well as variable thruster jets for attitude control.

## Project specifications

	Assigned	Modification	Motivation
Platform	Microsat (10-100 kg)		
Attitude parameters	Quaternions		
Mandatory sensor	Star Sensor	Added gyroscope	Obtain angular velocities in de-tumbling mode
Actuators	Variable thrust Jets		

## Task distribution

Surname	Name	Role
Coppola	Riccardo	DKE, Star Sensor, Gyro, Control
Corbo	Nicolò	DKE, Structure, Simulink Integration, Monte Carlo
Jönsson	Jonathan	DKE, QUEST Attitude Determination, Control
Spitalieri	Martina	DKE, Star Sensor, Actuators, Orbit

---

# Contents

<b>1</b>	<b>Introduction and mission requirements</b>	<b>1</b>
<b>2</b>	<b>Satellite Model</b>	<b>1</b>
2.1	External Surfaces Model . . . . .	2
2.2	Structural Model . . . . .	3
<b>3</b>	<b>Attitude dynamics and kinematics</b>	<b>4</b>
<b>4</b>	<b>Disturbance torques modeling</b>	<b>4</b>
<b>5</b>	<b>Sensors</b>	<b>6</b>
5.1	Star Sensor . . . . .	6
5.2	Fiber Optic Gyroscope . . . . .	7
<b>6</b>	<b>Attitude Determination</b>	<b>7</b>
<b>7</b>	<b>Control</b>	<b>8</b>
7.1	State space models . . . . .	8
7.1.1	Detumbling . . . . .	9
7.1.2	Slew Maneuver . . . . .	9
7.1.3	3-axis tracking . . . . .	10
7.2	LQR-method . . . . .	11
<b>8</b>	<b>Actuators</b>	<b>11</b>
<b>9</b>	<b>Results</b>	<b>12</b>
9.1	Attitude and pointing error . . . . .	12
9.2	Angular velocity . . . . .	14
9.3	Mass Properties . . . . .	14
9.4	Actuators . . . . .	14
9.5	Statistical Performance Analysis - Monte Carlo . . . . .	15
9.5.1	Simulation Introduction . . . . .	15
9.5.2	Results Analysis . . . . .	16
9.5.3	Conclusion . . . . .	18
	<b>References</b>	<b>19</b>

# 1. Introduction and mission requirements

Since the assigned spacecraft was a microsat ranging from 10 to 100 kg, the CE-SAT-IE (Compact Earth-Observation Satellite-1e) was chosen. It is a small, high-performance Earth-observation satellite developed by Canon Electronics Inc. as part of the company's broader CE-SAT series. Its designated mission is Earth observation and imaging for various applications, including disaster monitoring, urban planning, and agriculture; moreover, its objective was technology validation for potential use in larger satellites or commercial applications.

In this project a similar but simplified model of CE-SAT-IE was considered, including its prescribed orbit, whose orbital parameters are listed in Table 1.1. As these parameters were calculated through downloaded ephemerides on day 10/12/2024, the true anomaly relative to 10/12/2024 00:00:00 was considered as the initial true anomaly at release from launcher <sup>(1)</sup>.

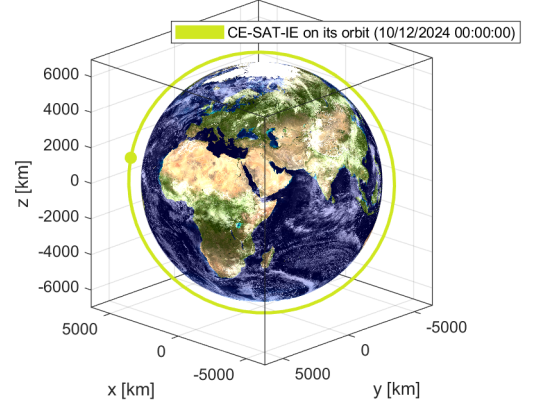


Figure 1.1: CE-SAT-IE orbit

Semi-major axis [km]	Eccentricity [-]	Inclination [deg]
7041	0.0020	98.2
RAAN [deg]	Argument of pericentre [deg]	True anomaly (release) [deg]
39.41	109.4	195.6

Table 1.1: CE-SAT-IE orbital parameters

Concerning the workflow of the model design, a block scheme represents the overall model through simplified blocks (see Figure 1.2).

The following parameters and requirements were selected as a consequence of similarity with the actual mission requirements of CE-SAT-IE, adapting to the assumptions which are mentioned throughout the report. As stated above, the mission of the satellite is to carry on Earth observation and Earth imaging: therefore, the object to point and the pointing direction are therefore the camera lens to be aligned with the Nadir axis, corresponding to the yaw axis in the LVLH frame. The LVLH frame has been rotated 90° to ensure that the rotation around the pitch axis is the correct one. The LVLH frame is setup as the following: x-axis (pitch), y-axis (roll), and z-axis (-yaw). Since the payload includes a camera that has to generate accurate and steady pictures, the pointing accuracy is chosen to be 0.1° - 0.5°, accordingly to the control precision derived from a three-axis control where the control torques are generated by variable thrust jets, where thrust can therefore be modulated. As for the control modes included in this design, the following sequence of events is taken into account:

- Orbit insertion and de-tumbling: considering a random attitude and high angular velocity derived from the launcher release, the control is in charge of slowing the rotational motion of the spacecraft
- Attitude acquisition and slew manoeuvre: once the spacecraft is rotationally stable, the star sensor is in charge of aiding in the attitude determination through his measurements to start determining its attitude at each timestep; once the spacecraft attitude is known at each timestep of the simulation, the control is in charge of acting the thrusters in such a way to reach the pointing requirements
- Tracking (Normal mode): used for the most part of the mission, the control torques are only in charge of dealing eventually with external or internal disturbances

<sup>1</sup> Note: orbital parameter derived through TLEs (Space-Track.org), ephemerides (NASA Horizon) and calculations on Matlab®

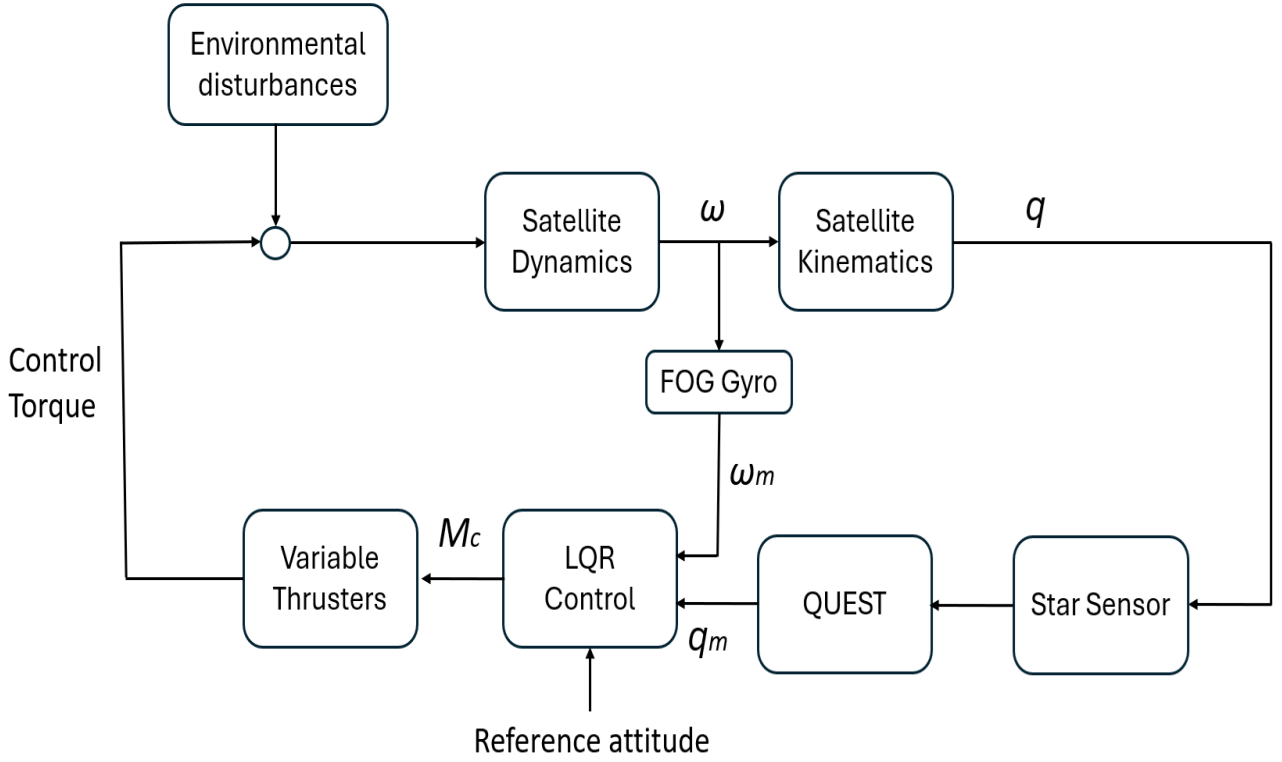


Figure 1.2: ADCS Block Scheme

## 2. Satellite Model

After choosing our satellite, with similar characteristics to the assigned project parameters, we started to model all the aspects that play a role into our attitude and dynamic analysis. For that goal, at least two satellite models are required:

- External Surfaces Model for the computation of the Solar Radiation Pressure and Aerodynamic Drag. Discretizing the faces, identified by the normal unit vector, area, and reflective properties.
- General Structural Model for the computation of center-of-mass position and inertia matrix. This model needs to account for the presence of fuel consumption due to thruster activity and such changes at every time.

For every information we weren't able to find on official sources, like the exact component mass and disposition, we choose to use a plausible estimation.

### 2.1 External Surfaces Model

Our discrete basic unit, used in modeling every complex shape, is a simple rectangular plate, characterized in Matlab by the coordinates of its vertices and the reflective coefficients. We decided to place the origin of the reference system at the geometrical center of the parallelepiped of the main structure. The center-of-mass instead requires the later explained Structural Model, to compute it at every time step.

The model includes 3 types of plates, differentiated by the reflective properties. The vector of the coefficients, whose sum must be one, is composed of the total reflection coefficient, the diffusive reflection coefficient, and the absorption coefficient, each related to the omonimous phenomenon.

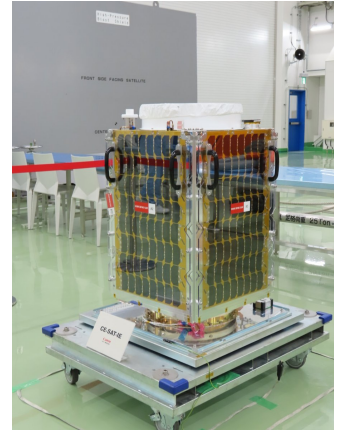


Figure 2.1: Real Satellite

Structural Element	Characteristics	Coefficients
Structural Plates	Load absorption and smooth, reflective surface	[0.6 0.1 0.3]
Solar Panels	Rays absorption for a near perfect energy conversion	[0.1 0.1 0.8]
Mirror Hole	Octagon model of a circle channeling all rays for the photo	[0.01 0.01 0.98]

Table 2.1: Surface Model Description

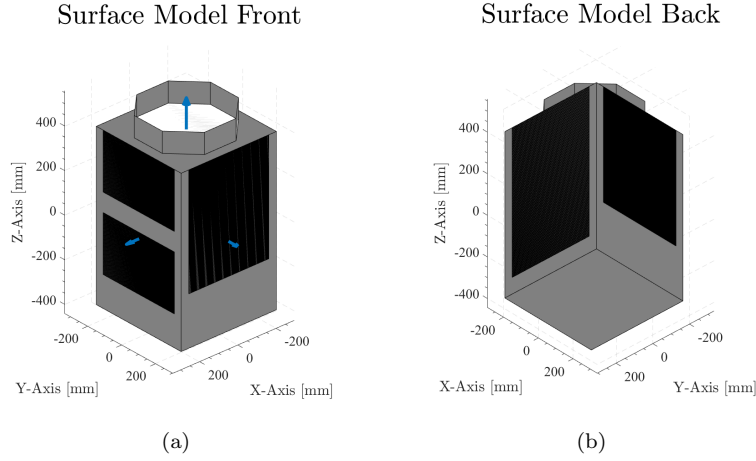


Figure 2.2: Surface Model

## 2.2 Structural Model

Considering the unavailability of a CAD file describing the specific structure of our satellite and the arrangement of its components, we relied on images obtained from official websites [1] to manually construct a model using Solidworks software. This choice is also useful since we are able, once we know the material composition of each part of a specific assembly, to compute both the center-of-mass position and the corresponding inertia matrix.

For reference, a simpler model can be obtained from a uniform and symmetric parallelepiped centered into the reference frame origin. The mass of the spacecraft and the global dimensions, found on the official site, are respectively  $m = 80 \text{ Kg}$  and *dimensions* :  $50\text{cm} \times 50\text{cm} \times 80\text{cm}$ .

By manually constructing the model, we can reduce the level of approximation associated with our structure, despite being constrained by certain factors. First and foremost, the structure must still be arbitrarily discretized into simpler solid shapes, composed of homogeneous materials whose properties are estimated and identified by us. Secondly, the structure must be designed in two versions: one with a full propellant tank and one with an empty tank, as our satellite uses thrusters as its propulsion system. The results for the three structures are listed in Table 2.2.

Model Type	Baricenter Position [m]	Mass [kg]	Inertia Matrix [ $\text{kg}/\text{m}^2$ ]
Reference Structure	$\begin{bmatrix} 0 \\ 0 \\ 0 \end{bmatrix}$	80	$\begin{bmatrix} 5.93 & 0 & 0 \\ 0 & 5.93 & 0 \\ 0 & 0 & 3.33 \end{bmatrix}$
Full Structure	$\begin{bmatrix} 6 \times 10^{-4} \\ -5.6 \times 10^{-3} \\ 3.6 \times 10^{-3} \end{bmatrix}$	80	$\begin{bmatrix} 7.687 & 2.673 \times 10^{-4} & 3.324 \times 10^{-3} \\ 2.673 \times 10^{-4} & 7.601 & 3.837 \times 10^{-2} \\ 3.324 \times 10^{-3} & 3.837 \times 10^{-2} & 5.423 \end{bmatrix}$
Empty Structure	$\begin{bmatrix} 6 \times 10^{-4} \\ -5.6 \times 10^{-3} \\ 1.1 \times 10^{-2} \end{bmatrix}$	70	$\begin{bmatrix} 6.701 & 2.460 \times 10^{-4} & 2.695 \times 10^{-3} \\ 2.460 \times 10^{-4} & 6.623 & 3.685 \times 10^{-2} \\ 2.695 \times 10^{-3} & 3.685 \times 10^{-2} & 4.839 \end{bmatrix}$

Table 2.2: Satellite Structural Models

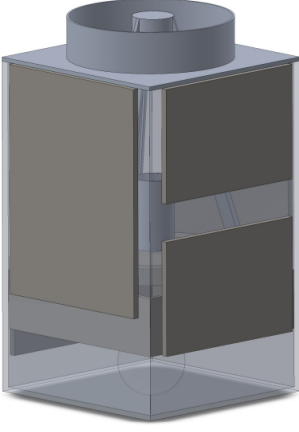


Figure 2.3: Structure Model

The first observable phenomenon is the loss of correspondence between the geometric body axes and the principal axes of inertia, evidenced by the non-zero values of the inertia products in the matrices. However, considering their order of magnitude, these quantities can be deemed negligible with minimal loss of precision and can therefore be treated as effectively zero. Compared to the reference model, we also observe a non-negligible increase in the structure's moment of inertia. This is primarily due to the placement of most components farther from the center of mass in our model, to accommodate the camera cavity at the center of the structure. This numerical results are therefore entirely justifiable. Furthermore, examining the results, we observe that the changes between the initial and final models, given the substantial amount of fuel onboard relative to the duration of the mission, are largely negligible. Nevertheless, for the sake of generality in our model, we have included an algorithm for the structural evolution of the satellite. This algorithm, leveraging specific impulse and actuator activity, is capable of calculating the evolution of the satellite's mass properties based on linear interpolation between the initial and final structures (noting that these

possess the property of linearity with respect to mass).

### 3. Attitude dynamics and kinematics

The rotational dynamics of the satellite is described by Euler's equations for a simple spin satellite. [2]

$$\begin{cases} I_x \dot{\omega}_x = (I_y - I_z) \omega_y \omega_z + \underline{M}_x \\ I_y \dot{\omega}_y = (I_z - I_x) \omega_z \omega_x + \underline{M}_y \\ I_z \dot{\omega}_z = (I_x - I_y) \omega_x \omega_y + \underline{M}_z \end{cases}$$

These equations were modeled through Simulink blocks and numerically integrated. The terms  $\underline{M}_x$ ,  $\underline{M}_y$  and  $\underline{M}_z$  represent the disturbances and control torques around the satellite's axes and  $I_x$ ,  $I_y$ ,  $I_z$  are the principal moments of inertia of the satellite. As imposed by the project specifications, attitude modeling was carried out exploiting quaternions kinematics. [2]

$$\dot{\underline{q}}(t) = \frac{1}{2} \Omega(t) \underline{q}(t) \quad \text{where} \quad \Omega(t) = \begin{bmatrix} 0 & \omega_z & -\omega_y & \omega_x \\ -\omega_z & 0 & \omega_x & \omega_y \\ \omega_y & -\omega_x & 0 & \omega_z \\ -\omega_x & -\omega_y & -\omega_z & 0 \end{bmatrix} \quad (3.1)$$

Quaternions are normalized at each step of the simulation. Finally, a conversion block was added; the reason is that for some other model blocks (for instance the star sensor) an easier modeling was possible exploiting direction cosine matrices instead of quaternions. Therefore, since as specified above the kinematics was imposed to be computed via quaternions, direction cosine matrices are computed after through the DCM-quaternion conversion [2]

$$\underline{A} = (\underline{q}_4^2 - \underline{q}^T \underline{q}) \underline{I} + 2 \underline{q} \underline{q}^T - 2 \underline{q}_4 [\underline{q}^\wedge] \quad \text{where} \quad [\underline{q}^\wedge] = \begin{bmatrix} 0 & -q_3 & q_2 \\ q_3 & 0 & -q_1 \\ -q_2 & q_1 & 0 \end{bmatrix} \quad (3.2)$$

### 4. Disturbance torques modeling

Four environmental disturbances have been analyzed in this model, specifically the ones due to Earth's magnetic field and gravity field, but also the Solar Radiation Pressure and the air drag resistance (see Table 4.1. A preliminary estimation of the magnitude of the four was calculated using the reference formulas <sup>1</sup> and was subsequently refined through a statistical analysis of the simulations. (see Chapter 9.4)

<sup>1</sup>See page 18, section 09 - SRP and air drag - [2]

As it was already clear by estimations, all of them contribute with little to no effect on the spacecraft; among the four, the gravity gradient was taken into account in the model, as well as the magnetic field and the SRP since they share a similar value. For its very low value, the air drag was not included in the Simulink model, stating therefore the assumption of drag torque to be completely negligible in the case at hand: considering the structure of the satellite, with no open or extended surfaces and its little dimensions, it was considered a reasonable conclusion.

Disturbance	Simulation
Gravity gradient	3.822e-7
Magnetic field	1.891e-6
SRP	2.404e-7
Air drag	1.324e-16

Table 4.1: Environmental disturbances values

### Earth magnetic field

The presence of electrical and electronic components on our satellite leads to interactions with the magnetic field naturally generated by the Earth. With a certain degree of approximation, the Earth's magnetic field can be modeled as a uniform dipole, and its interaction with the residual internal dipole generated by the satellite can be calculated. This approximation is considered valid and sufficiently accurate at very high altitudes, where the effects of magnetic field inhomogeneity are negligible. However, considering our low altitude, we must rely on the most accurate model available to us, the IGRF (*International Geomagnetic Reference Field*).

The model calculates the magnetic field as the spatial gradient of a scalar potential given by the following formula, that can be expanded up to order  $k = 13$ , looking for the highest precision, using tabled Gaussian Coefficients  $g$  e  $h$ , and iteratively computed Schmidt quasi-normalize Legendre function and its derivative  $P$ :

$$V(r, \theta, \phi) = R_{\oplus} \sum_{n=1}^k \left( \frac{R_{\oplus}}{r} \right)^{n+1} \sum_{m=0}^n (g_n^m \cos(m\phi) + h_n^m \sin(m\phi)) P_n^m(\theta) \quad (4.1)$$

The overall interaction with the satellite is consequently calculated as the cross product of the residual induced dipole moment (our estimation) and the external magnetic field in body frame.

$$\underline{M}_{mag} = \underline{D} \times \underline{B}^{body} \quad \underline{D} = [0.05 \ 0.05 \ 0.05] Am^2 \quad (4.2)$$

### Gravity gradient

Since Earth's gravity field is not uniform and its value depends on the distance from Earth, the gravity gradient torque acting on the satellite was modeled through

$$\underline{M}_{GG} = \frac{3GM_{\oplus}}{r^3} \begin{bmatrix} (I_z - I_y)c_3c_2 \\ (I_x - I_z)c_1c_3 \\ (I_y - I_x)c_2c_1 \end{bmatrix} \quad (4.3)$$

where  $G$  is the universal gravitational constant,  $M_{\oplus}$  is the mass of Earth,  $r$  is the distance of the satellite from the centre of Earth, and  $c_i$  can be obtained by rotating the vector  $[1 \ 0 \ 0]^T$  using the direction cosine matrix  $A_{B/L}$ .

### Solar Radiation Pressure

Solar radiation intensity varies with the inverse square distance from the source and the average pressure can be evaluated as  $P = \frac{F_e}{c}$  where  $F_e$  is the power per unit surface whereas  $c$  is the speed of light; the force on the single flat panel and the corresponding torque are

$$\underline{F}_i = -PA_i(\hat{S}_b - \hat{N}_{bi})[(1 - \rho_s)\hat{S}_b + (2\rho_s(\hat{S}_b - \hat{N}_{bi}) + \frac{2}{3}\rho_d)\hat{N}_{bi}], \quad \hat{S}_b = A_{B/N}\hat{S}_i \quad \text{and} \quad \underline{T}_{SRP} = \underline{r}_i \wedge \underline{F}_i \quad (4.4)$$



# 5. Sensors

## 5.1 Star Sensor



Figure 5.1: Jena-Optronik ASTRO APS

The main attitude determination sensor on-board was assigned to be a star sensor: the Jena-Optronik ASTRO APS Star Sensor was considered in this analysis. In the framework of a simplified model, the Simulink Star Sensor block takes as inputs the attitude computed in the real system (in the Kinematics block) as well as the sensor mounting matrix (considered from sensor to body frame,  $A_{B/S}$ ). At first, the idea was to input also a star catalog, specifically downloaded from Vizier Hipparcos: for each star, its ID, its brightness magnitude measured in Johnson V-band were downloaded and its right ascension, declination and inertial unit vector (in ECI) were computed. However, the number of stars in the catalog was too vast to implement it in a reasonable simulation time, while on the other hand randomly excluding some stars would create "holes" in the sensor FOV. How it was managed to model a similar behavior was to generate random stars in the FOV at each timestep: based on the assumption that there are always at least 5 stars in the FOV (diminished by a certain tolerance to avoid border effects) at each timestep, exploiting a random generation of "points" and correspondent random brightness values, 7 different "stars" are obtained each timestep, which then undergo a detection algorithm.

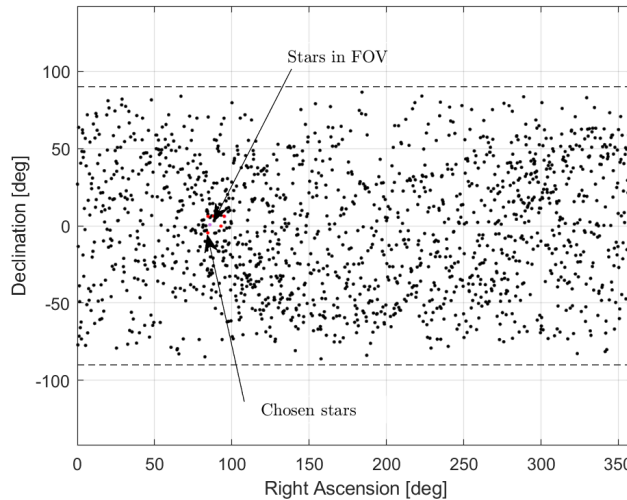


Figure 5.2: Sky and stars choice representation

For clarity, the sensor frame is considered here with its y-axis correspondent to the sensor boresight, the x-axis rightwards and consequently the z-axis determined with the usual right-hand rule. The detection algorithm based on Liebe's 1992 star search process algorithm detects the brightest star among those present in the FOV (that were generated randomly), then through trigonometric considerations the 4 stars closest to it are identified [3].

Thanks to this process, the star sensor is able to determine at each time step of the simulation five stars directions both in its own sensor frame as well as in the inertial frame (thanks to the matrix  $A_{S/N}$  which is computed at each timestep from the real attitude given by the Kinematics). Exploiting the constant mounting matrix, the five stars directions can also be rotated in the satellite's body frame to then be exploited in Attitude Determination. Obviously, a performance model of the sensor was included: from the datasheet [4], a bias error as well as random errors were taken into account. Moreover, a misalignment error of 0.5 deg around the sensor z-axis was considered, since it could derive from an incorrect mounting of the sensor itself or from the lens being slightly askew. The simulation data are presented in Table 5.2.

Mounting matrix ( $A_{S/B}$ )	Misalignment error	FOV	FOV border tolerance	Bias
$\begin{bmatrix} 0 & 0 & -1 \\ 1 & 0 & 0 \\ 0 & -1 & 0 \end{bmatrix}$	$\begin{bmatrix} 0.99999 & 0.00087 & 0 \\ -0.00087 & 0.99999 & 0 \\ 0 & 0 & 1 \end{bmatrix}$	20 deg	0.5 deg	$\sim 0.01$ deg

Table 5.1: Star Sensor - simulation data

## 5.2 Fiber Optic Gyroscope

The team initially developed a Fiber Optic Gyroscope as a secondary sensor for the cases in which the main star sensor is unable to provide its data, in particular referring to the de-tumbling manoeuvre when the slew rates excess the limit of the star sensor. In the final model it was decided to maintain the sensor as it could provide precise measurements of the angular velocities, useful for the 3-axis tracking phase. The Gran Stal Solutions GS-FOG70A was the gyroscope considered in this analysis. For this project the team developed a performance model of the sensor, relying on the information present in the datasheet when available, and making reasonable estimations otherwise [5]. The misalignment error was represented as a rotation of  $0.1^\circ$  around its Z axis. The non-orthogonality intrinsic error of the gyroscope was modeled as a combination of rotations around the 3 sensor axes of  $0.05^\circ$ , an indicative value for high precision gyros. Finally the bias offset was assumed to be  $0.01^\circ/\text{sec}$  and it represents a constant and slow shift of the measurements acting at each timestep. The the high precision of GS-FOG70A leads to not visible effects neither to the bias in-run stability nor to Rate Random Walk errors for the desired time of simulation.

Misalignment error	Non Orthogonality error	Bias
$\begin{bmatrix} 0.99999 & 0.00174 & 0 \\ -0.00174 & 0.99999 & 0 \\ 0 & 0 & 1 \end{bmatrix}$	$\begin{bmatrix} 0.99999 & 0.00087 & 0.00087 \\ -0.00087 & 0.99999 & 0.00087 \\ -0.00087 & -0.00087 & 0.99999 \end{bmatrix}$	$\sim 0.01$ deg/sec

Table 5.2: Star Fiber optic Gyroscope - simulation data

## 6. Attitude Determination

QUEST was chosen due to it estimating the attitude directly in quaternion format which avoids running into singularities. However, the sign ambiguity is still necessary to take into consideration due to the fact that any given rotation has two possible quaternion representations. This is handled through checking the direction with a dot product between the current estimated quaternion and the estimated quaternion in the previous timestep. This way if the dot product is negative, showing opposite directions, it can be corrected into the right direction with multiplying the estimated quaternion in the current timestep with -1. The sensor provides 5 vector measurements which is well above the minimum required of 2 vector measurements for the use of this method. Selecting QUEST as the attitude determination algorithm, Wahba's problem is the function that needs to be minimized:

$$J(A) = \sum_{i=1}^N \alpha_i - q^T K q \quad (6.1)$$

This leads to the obvious conclusion of the function that needs to be maximised so that Wahba's problem becomes minimized:

$$\tilde{J}(A) = q^T K q \quad (6.2)$$

K is built up as the following:

$$B = \sum_{i=1}^N \alpha_i s_i v_i^T \quad (6.3)$$

$$S = B^T + B \quad (6.4)$$

$$z = [b_{23} - b_{32}, b_{31} - b_{13}, b_{12} - b_{21}]^T \quad (6.5)$$

Where  $b_{xx}$  represents the components from matrix B in (6.3).

$$\sigma = \text{tr}(B) \quad (6.6)$$

$$K = \begin{bmatrix} S - \sigma I & z \\ z^T & \sigma \end{bmatrix} \quad (6.7)$$

$s_i$  represents the vector of direction to the star in sensor frame while  $v_i$  represents the vector of direction to the star in the inertial frame. In order to maximize (6.2) the following constraint must be applied with the associated Lagrange multiplier  $\lambda$ :

$$q^T q = 1 \quad (6.8)$$

Further, the following function which is maximised with no constraints is evaluated:

$$\tilde{G} = q^T K q - \lambda(q^T q - 1) \quad (6.9)$$

Taking the gradient of (6.9) and equating it to zero:

$$K q = \lambda q \quad (6.10)$$

Putting (6.10) into (6.2):

$$\tilde{J}(A) = q^T K q = q^T \lambda q \quad (6.11)$$

The maximum value of the cost function therefore relates to the maximum eigenvalue of matrix K. Therefore the eigenvector corresponding to that eigenvalue can be seen as the optimal estimated quaternion.

## 7. Control

The control is designed with state space models and the linear quadratic regulator algorithm (LQR). Using this approach for the control over pole placement allows for tuning the response of the system more intuitively. Rather than trying to figure out how much the poles would need to be moved to tune the system a certain way, the LQR moves the poles with respect to the response that is wanted. The simulation is initiated with a initial value around each axis to simulate any angular velocity of the satellite while being released into space before the detumbling process starts. Thereafter the slew maneuver and the 3-axis tracking is triggered at later times with certain thresholds. The detumbling process will be the starting point of the simulation where there is a gain matrix pushing the angular velocities down to zero. A threshold of  $0.573^\circ/\text{s}$  magnitude of the angular velocity has been set up for when to switch from detumbling to the slew maneuver which corresponds to when the star sensor can be activated ( $< 3^\circ/\text{s}$ ). The slew maneuver being a rest to rest motion, has a new gain matrix that maintains the angular velocity going to zero but also minimizes the error between the estimated attitude from the sensor and a fixed snapshot from the target reference frame in the time instant of going from detumbling to slew maneuver. The gravity gradient can be linearized which is why it is included in the model, whereas the other disturbances are neglected in the moving frame due to complexity. The threshold for the switch from slew maneuver to the 3-axis tracking relates to an average close enough to zero of the off-diagonal values in the error matrix 7.10. Once the 3-axis tracking is triggered it will continue until the end of the simulation with its own gain matrix, keeping the satellite nadir pointing as well as establishing the average rotational velocity of the satellite in the pitch axis and zero in the roll and yaw axis.

### Target Reference Frame

Our reference frame, named LVLH\*, used as the tracking target and extrapolated as the slew direction, is defined as a  $90^\circ$  rotation of the LVLH frame around the roll axis. In the rotated frame, the z-direction (LVLH pitch) corresponds to the vector connecting the satellite to the Earth's center, the x-direction (LVLH yaw) aligns with the orbital angular momentum unit vector, and the y-direction is defined as the LVLH roll. Consequently, the rotation matrix relative to the body frame is as follows:

$$A_{B/L^*} = \begin{bmatrix} \hat{h}_{orbit} & \hat{h}_{orbit} \times \hat{r} & -\hat{r} \end{bmatrix} \quad (7.1)$$

### 7.1 State space models

To represent our models in state space [2] the following equation is used, where  $x$  represents the state, and  $u$  represents the input:

$$\dot{x} = Ax + Bu \quad (7.2)$$

Euler equations to be linearized:

$$\dot{x} = f_1(x, u, t) \rightarrow \begin{cases} \dot{w}_x = -\frac{I_z - I_y}{I_x} w_z w_y + \frac{1}{I_x} M_x \\ \dot{w}_y = -\frac{I_x - I_z}{I_y} w_x w_z + \frac{1}{I_y} M_y \\ \dot{w}_z = -\frac{I_y - I_x}{I_z} w_y w_x + \frac{1}{I_z} M_z \end{cases} \quad (7.3)$$

Euler equations with gravity gradient to be linearized:

$$\dot{x} = f_2(x, u, t) \rightarrow \begin{cases} \dot{w}_x = 3n^2(I_z - I_y)c_3c_2 - \frac{I_z - I_y}{I_x} w_z w_y + \frac{1}{I_x} M_x \\ \dot{w}_y = 3n^2(I_x - I_z)c_1c_3 - \frac{I_x - I_z}{I_y} w_x w_z + \frac{1}{I_y} M_y \\ \dot{w}_z = 3n^2(I_y - I_x)c_2c_1 - \frac{I_y - I_x}{I_z} w_y w_x + \frac{1}{I_z} M_z \end{cases} \quad (7.4)$$

### 7.1.1 Detumbling

To attain zero angular velocities during detumbling the equilibrium condition are set as:

$$\bar{w}_x = \bar{w}_y = \bar{w}_z = 0 \quad (7.5)$$

Knowing the equilibrium condition we can now linearize the equation (7.3) to find A and B seen in (7.2):

$$A = \left. \frac{\partial f}{\partial x} \right|_{\substack{x=\bar{x} \\ u=\bar{u}}} = \begin{bmatrix} 0 & 0 & 0 \\ 0 & 0 & 0 \\ 0 & 0 & 0 \end{bmatrix} \quad (7.6)$$

$$B = \left. \frac{\partial f}{\partial u} \right|_{\substack{x=\bar{x} \\ u=\bar{u}}} = \begin{bmatrix} \frac{1}{I_x} & 0 & 0 \\ 0 & \frac{1}{I_y} & 0 \\ 0 & 0 & \frac{1}{I_z} \end{bmatrix} \quad (7.7)$$

(7.6) and (7.7) in (7.2) gives the linearized euler equations in state space form:

$$\begin{bmatrix} \dot{w}_x \\ \dot{w}_y \\ \dot{w}_z \end{bmatrix} = \begin{bmatrix} 0 & 0 & 0 \\ 0 & 0 & 0 \\ 0 & 0 & 0 \end{bmatrix} \begin{bmatrix} w_x \\ w_y \\ w_z \end{bmatrix} + \begin{bmatrix} \frac{1}{I_x} & 0 & 0 \\ 0 & \frac{1}{I_y} & 0 \\ 0 & 0 & \frac{1}{I_z} \end{bmatrix} \begin{bmatrix} M_x \\ M_y \\ M_z \end{bmatrix} \quad (7.8)$$

Controllability:

$$Q = [B \ AB \ A^2B] \quad (7.9)$$

The rank of Q is 3 which matches with the number of states, therefore the system is controllable.

### 7.1.2 Slew Maneuver

Having considered small rotations between the body fixed frame and LVLH\* frame, there are three small angles  $\alpha_x, \alpha_y, \alpha_z$  that can be seen coupled to the angular velocity. Therefore the rotation matrix showing the relative attitude between the satellite and the LVLH\* frame becomes:

$$A_{B/L^*} = \begin{bmatrix} -\alpha_y & \alpha_z & -1 \\ \alpha_x & 1 & \alpha_z \\ 1 & -\alpha_x & -\alpha_y \end{bmatrix} \quad (7.10)$$

Assuming the angular velocity of the still frame of the LVLH\* frame is zero the angular velocity in body frame can be described as:

$$\begin{bmatrix} w_x \\ w_y \\ w_z \end{bmatrix} = \begin{bmatrix} \dot{\alpha}_x \\ \dot{\alpha}_y \\ \dot{\alpha}_z \end{bmatrix} + \begin{bmatrix} -\alpha_y & \alpha_z & -1 \\ \alpha_x & 1 & \alpha_z \\ 1 & -\alpha_x & -\alpha_y \end{bmatrix} \begin{bmatrix} 0 \\ 0 \\ 0 \end{bmatrix} \quad (7.11)$$

Knowing that  $c_1, c_2$ , and  $c_3$  are directions cosines in the radial direction of the principal axis:

$$\begin{bmatrix} c_1 \\ c_2 \\ c_3 \end{bmatrix} = \begin{bmatrix} -\alpha_y & \alpha_z & -1 \\ \alpha_x & 1 & \alpha_z \\ 1 & -\alpha_x & -\alpha_y \end{bmatrix} \begin{bmatrix} 0 \\ 0 \\ -1 \end{bmatrix} = \begin{bmatrix} 1 \\ -\alpha_z \\ \alpha_y \end{bmatrix} \quad (7.12)$$

Taking the time derivative of (7.11):

$$\begin{cases} \dot{w}_x = \ddot{\alpha}_x \\ \dot{w}_y = \ddot{\alpha}_y \\ \dot{w}_z = \ddot{\alpha}_z \end{cases} \quad (7.13)$$

(7.11), (7.12) and (7.13) in (7.4) and neglecting terms with two angles or derivatives the following linearized equation is found:

$$\begin{cases} I_x \ddot{\alpha}_x = M_x \\ I_y \ddot{\alpha}_y = M_y \\ I_z \ddot{\alpha}_z = M_z \end{cases} \quad (7.14)$$

Neglecting viscous damping the angular velocity can be set as  $\underline{w} = \dot{\underline{\alpha}}$  as well as  $\underline{\alpha} = \ddot{\underline{\alpha}}$ , and thereafter put (7.14) in a state space form as the following:

$$\begin{bmatrix} \dot{w}_x \\ \dot{w}_y \\ \dot{w}_z \\ w_x \\ w_y \\ w_z \end{bmatrix} = \begin{bmatrix} 0 & 0 & 0 & 0 & 0 & 0 \\ 0 & 0 & 0 & 0 & 0 & 0 \\ 0 & 0 & 0 & 0 & 0 & 0 \\ 1 & 0 & 0 & 0 & 0 & 0 \\ 0 & 1 & 0 & 0 & 0 & 0 \\ 0 & 0 & 1 & 0 & 0 & 0 \end{bmatrix} \begin{bmatrix} w_x \\ w_y \\ w_z \\ \alpha_x \\ \alpha_y \\ \alpha_z \end{bmatrix} + \begin{bmatrix} \frac{1}{I_x} & 0 & 0 \\ 0 & \frac{1}{I_y} & 0 \\ 0 & 0 & \frac{1}{I_z} \\ 0 & 0 & 0 \\ 0 & 0 & 0 \\ 0 & 0 & 0 \end{bmatrix} \begin{bmatrix} M_x \\ M_y \\ M_z \\ 0 \\ 0 \\ 0 \end{bmatrix} \quad (7.15)$$

Controllability:

$$Q = [B \ AB \ A^2B \ A^3B \ A^4B \ A^5B] \quad (7.16)$$

The rank of Q is 6 which matches with the number of states, therefore the system is controllable.

### 7.1.3 3-axis tracking

Switching to the tracking phase the fact that the LVLH\* frame is moving has to be taken into consideration. This changes (7.11) into:

$$\begin{bmatrix} \dot{w}_x \\ \dot{w}_y \\ \dot{w}_z \end{bmatrix} = \begin{bmatrix} \dot{\alpha}_x \\ \dot{\alpha}_y \\ \dot{\alpha}_z \end{bmatrix} + \begin{bmatrix} -\alpha_y & \alpha_z & -1 \\ \alpha_x & 1 & \alpha_z \\ 1 & -\alpha_x & -\alpha_y \end{bmatrix} \begin{bmatrix} n \\ 0 \\ 0 \end{bmatrix} \quad (7.17)$$

Where  $n$  represents the average rotational velocity of the satellite in orbit:

$$n = \sqrt{\frac{\mu}{a^3}} \quad (7.18)$$

(7.13) becomes:

$$\begin{cases} \dot{w}_x = \ddot{\alpha}_x - \dot{\alpha}_y \cdot n \\ \dot{w}_y = \ddot{\alpha}_y + \dot{\alpha}_x \cdot n \\ \dot{w}_z = \ddot{\alpha}_z \end{cases} \quad (7.19)$$

The new linearized equation is found with (7.12), (7.17) and (7.19) in (7.4):

$$\begin{cases} I_x \ddot{\alpha}_x (I_z - I_y - I_x) n \dot{\alpha}_y + (I_z - I_y) n^2 \alpha_x = M_x \\ I_y \ddot{\alpha}_y (I_x + I_y - I_z) n \dot{\alpha}_x + (I_z - I_x) n^2 \alpha_y = 3n^2 (I_x - I_z) \alpha_y + M_y \\ I_z \ddot{\alpha}_z = -3n^2 (I_y - I_x) \alpha_z M_z \end{cases} \quad (7.20)$$

Simplifying the equation by setting:

$$\begin{cases} K_y = \frac{(I_z - I_y)}{I_x} \\ K_r = \frac{(I_z - I_x)}{I_y} \\ K_p = \frac{(I_y - I_x)}{I_z} \end{cases} \quad (7.21)$$

The following state space representation can be made of the linearized equation by neglecting the viscous damping as in the slew maneuver:

$$\begin{bmatrix} \dot{w}_x \\ \dot{w}_y \\ \dot{w}_z \\ w_x \\ w_y \\ w_z \end{bmatrix} = \begin{bmatrix} 0 & (1 - K_y)n & -K_y n^2 & 0 & 0 & 0 \\ (K_r - 1)n & 0 & 0 & 0 & -4K_r n^2 & 0 \\ 0 & 0 & 0 & 0 & 0 & -3K_p n^2 \\ 1 & 0 & 0 & 0 & 0 & 0 \\ 0 & 1 & 0 & 0 & 0 & 0 \\ 0 & 0 & 1 & 0 & 0 & 0 \end{bmatrix} \begin{bmatrix} w_x \\ w_y \\ w_z \\ \alpha_x \\ \alpha_y \\ \alpha_z \end{bmatrix} + \begin{bmatrix} \frac{1}{I_x} & 0 & 0 \\ 0 & \frac{1}{I_y} & 0 \\ 0 & 0 & \frac{1}{I_z} \\ 0 & 0 & 0 \\ 0 & 0 & 0 \\ 0 & 0 & 0 \end{bmatrix} \begin{bmatrix} M_x \\ M_y \\ M_z \\ 0 \\ 0 \\ 0 \end{bmatrix} \quad (7.22)$$

Controllability:

Using (7.16) again, the rank of  $Q$  for the 3-axis tracking system is 6 which matches with the number of states, therefore the system is controllable.

## 7.2 LQR-method

The LQR-method [2] was chosen due to having clear links between performance of the state and control expense in the form of thrust from the actuators, while at the same time creating a asymptotically stable system. The following cost function is used to provide an optimal solution:

$$J_0 = \frac{1}{2}x_f^T S x_f + \frac{1}{2} \int_0^{t_0} x^T (Q + P^T B R^{-1} B^T P) x dt \quad (7.23)$$

$Q$  and  $R$  are the weighting matrices penalizing the performance or control respectively.  $P$  is the solution to Riccati's equation,  $B$  is the matrix from the state space form of the model, and  $x_f$  is the final value of the transient part of the state. The gain matrix is directly connected through the following equation:

$$\bar{u} = K \bar{x} = -R^{-1} B^T P \bar{x} \quad (7.24)$$

MATLAB has a built-in function that allows for solving the cost function directly by providing the matrices  $A, B, Q$ , and  $R$ . Therefore there only needs tuning of the weighting matrices  $Q$  and  $R$  to retrieve a suitable gain matrix for each state space model. The values of  $Q$  and  $R$  was initially chosen through Bryson's rule:

$$\begin{cases} Q = \text{diag}(\frac{1}{x_{iMa}^2}) \\ R = \text{diag}(\frac{1}{u_{iMa}^2}) \end{cases} \quad (7.25)$$

This way the matrices can be set up through defining maximum deviations of the state and control to get a good initial estimate of the gain matrix  $K$ . The matrices were further tuned due to the need for penalizing the control and state performance to achieve the criterias regarding the total cost of fuel for the maneuvers as well as the maximum possible thrust from the actuators on each axis. The gain matrices for each phase are set up as the following.

Phase	Detumbling	Slew Maneuver	3-axis Tracking
<b>Gain Matrix</b>	$\bar{u} = K_1 \bar{x} = K_1 \begin{bmatrix} w_x \\ w_y \\ w_z \end{bmatrix}$	$\bar{u} = K_2 \bar{x} = K_2 \begin{bmatrix} w_x \\ w_y \\ w_z \\ \alpha_x \\ \alpha_y \\ \alpha_z \end{bmatrix}$	$\bar{u} = K_3 \bar{x} + \bar{w} \times J \bar{w} = K_3 \begin{bmatrix} w_x \\ w_y \\ w_z \\ \alpha_x \\ \alpha_y \\ \alpha_z \end{bmatrix} + \bar{w} \times J \bar{w}$

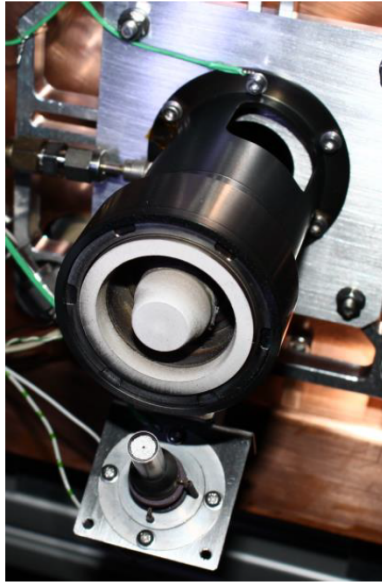
Table 7.1: Control Gain Matrices

## 8. Actuators

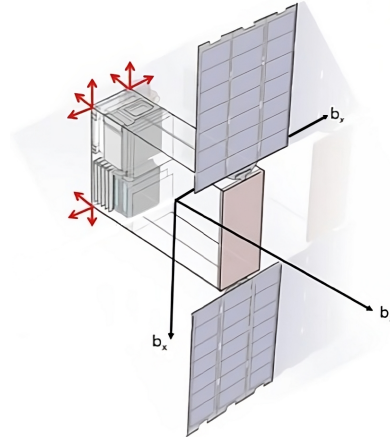
As for actuators, electric-propulsion thrusters were chosen, specifically the SITAEL HT100 exploiting the Hall Effect, which enabled a variable and modulated thrust. As for the configuration, a 12-thruster design was implemented, as depicted in Figure 8.1. The  $R$ -matrix was calculated exploiting the known position of each thruster, as well as the direction of its thrust but also the position at each timestep of the center of mass in body axes. From this, a vector  $\underline{f}$  is computed via the Moore-Penrose pseudo-inverse Simulink block<sup>1</sup> of the  $R$ -matrix and the control torque  $\underline{M}_c$  corrected through the  $\gamma \underline{\omega}$  factor, where each element represents the magnitude of the force each thruster needs to deliver.

$$\mathbf{R} = \begin{bmatrix} \underline{r}_1 \wedge \underline{d}_1 & \underline{r}_2 \wedge \underline{d}_2 & \dots & \underline{r}_{12} \wedge \underline{d}_{12} \end{bmatrix} \quad (8.1)$$

<sup>1</sup>See DSP System Toolbox



(a) SITAEL HT100



(b) 12 thrusters configuration

Figure 8.1: Actuators

$$\underline{f} = \mathbf{R}^* \underline{M}_c + \gamma \underline{\omega} \quad (8.2)$$

Obviously, a performance model of the actuators was added to account for mounting errors, switching-on and switching-off delays, as well as disturbances and noises. For the SITAEL HT100, the time constant for switching-on is mainly determined by the ionization of the propellant and stabilization of the plasma discharge: a typical value of  $\tau_{on} = 0.5s$  was considered. On the other hand, the switch-off time constant reflects the time required for the plasma discharge and thrust to decay after power is cut. A similar value of  $\tau_{off} = 0.5s$  was considered. Moreover, concerning the thrust efficiency, from the datasheet a value of 40% was used, as well as a negative bias of 0.5 mN and a scale factor of non-linearity of 27778 ppm (assuming a maximum deviation of 0.5 mN). Lastly, similarly to the star sensor, a misalignment error of 0.05 deg on every axis was considered for each thruster, as in the worst case scenario each thruster might be subjected to an error due to mounting or similar.

## 9. Results

The following chapter aims to illustrate the results obtained from the simulation, run over a full orbit of the satellite around the Earth, so for its orbital period of  $T_{orb} = 5879.7993$  s (approximated as 5880 s). The initial conditions for these results are  $\underline{\omega}_0 = [0.5 \ 0.5 \ 0.5]$  rad/s and  $\underline{q}_0 = [0 \ 0 \ 0 \ 1]$ .

### 9.1 Attitude and pointing error

This section is dedicated to the evolution in time of errors related to the attitude and angular velocity estimations, as well as the pointing performance during a single run of the simulation.

Figure 9.1 presents the errors in angular velocity and attitude. Such quantities are measured on-board through sensors and the attitude determination subsystem, hence the development of errors is an inevitable process. The attitude error is expressed in terms of magnitude of the Euler angle representing the rotation between the real and the sensed attitude. Such error is maintained beneath  $0.3^\circ$  for most of the simulation, which is considered a satisfactory level of accuracy. On the other hand the error in angular velocity after the slew manoeuvre is restricted to the order of magnitude of  $10^{-2}$  °/sec and it is maintained to such level throughout the entire simulation, thanks to the high precision of the fiber optic gyroscope.

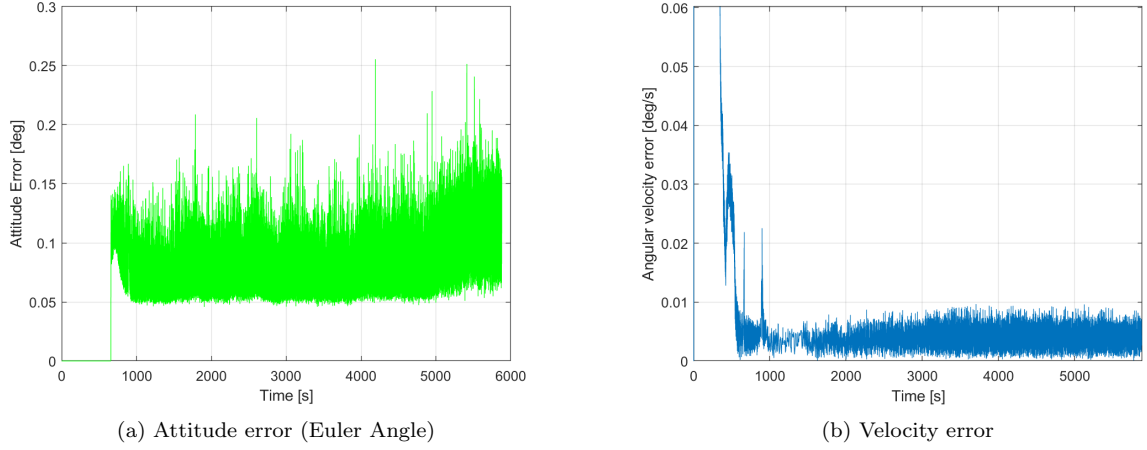


Figure 9.1: Dynamics-Kinematics error

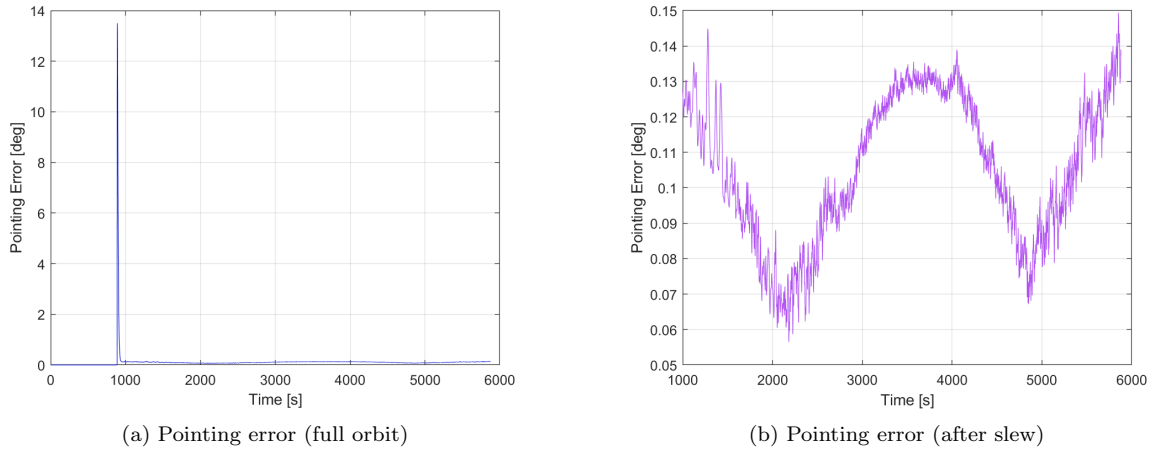


Figure 9.2: Pointing error

Figure 9.2 presents the errors achieved in terms of pointing in the nadir direction over time. As can be seen clearly in the full orbit pointing error, the satellite has no idea what attitude it has since the star sensor can't yet be activated. Once the detumbling process is over, which is in the peak of the graph, the star sensor can start obtaining an estimate of the attitude and the control can start aligning the satellite with the target attitude. Since the pointing error during the de-tumbling and slew manoeuvre may be many orders of magnitude higher than in the tracking, an alternative plot is presented to highlight the pointing error only during the 3-axis tracking phase. The performance of the system during the tracking satisfies the initial requirements of the mission, as the pointing error is maintained below  $0.5^\circ$  at every timestep of the simulation. This means that when the control system switches to the the 3-axis tracking the spacecraft follows properly the LVLH\* frame.



## 9.2 Angular velocity

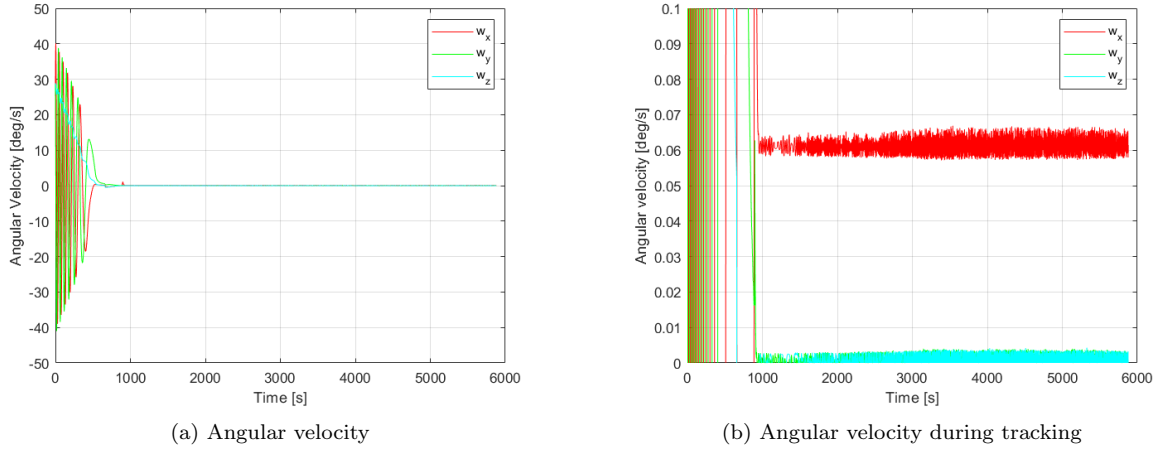


Figure 9.3: Angular velocity

As can be seen in 9.4 of the zoomed out figure of the angular velocity to the left, the angular velocity is pushed down to zero during the detumbling. While entering the slew maneuver there is a slight spike due to rotating the satellite into the correct attitude. Once tracking is initiated, the most important detail is seen in the right figure which is zoomed in on the angular velocity. The angular velocity around the pitch axis which is in our case around the x-axis, oscillates around the target angular velocity of  $n = 0.0630^\circ/s = 0.0011 \text{ rad/s}$  which is what we want. While also keeping the angular velocities of the roll and yaw axis close to zero to obtain a constant nadir pointing during orbit.

## 9.3 Mass Properties

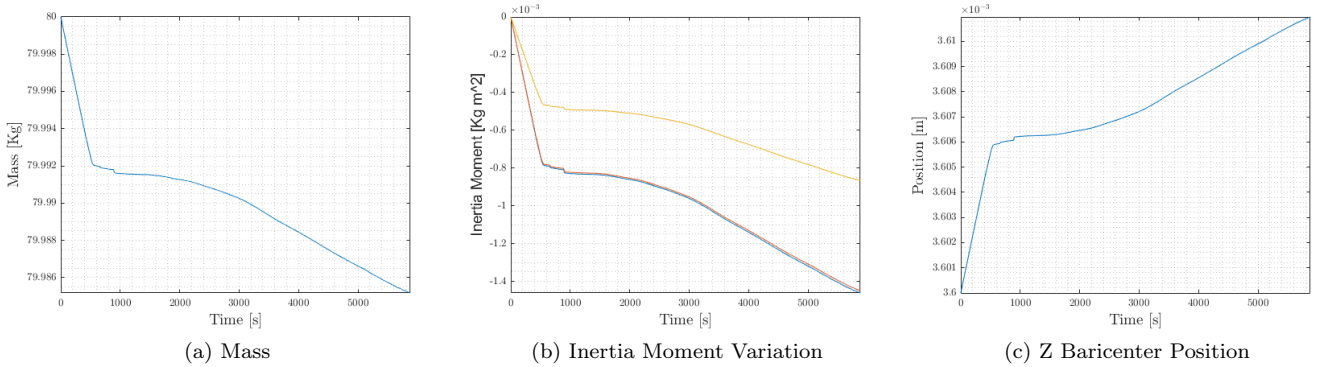


Figure 9.4: Mass, Inertia and Baricenter

Examining the variation in the mass properties of our model, several observations naturally arise. First, we note the extremely small differences over this extended period of time, making the effect entirely negligible. Second, we observe that the rate of variation is highly dependent on the phase of flight in which the system is operating, as the demands on the propulsion system change accordingly. The detumbling phase is clearly the most demanding, as it begins at high velocities, which are not encountered again later and incur a significant cost. Following an intermediate plateau during the slew phase, the demands rise again in the tracking phase, as the objective shifts to continuous stabilization and the mitigation of external disturbances. Only the z-position of the center of mass is represented, as the other positions remain unchanged due to symmetry considerations.

## 9.4 Actuators

The work of the chosen actuators in general proves to be effective; in the de-tumbling and slew manoeuvre phase, they are able to follow the desired torque with fair accuracy, proving that the chosen data (where not specified

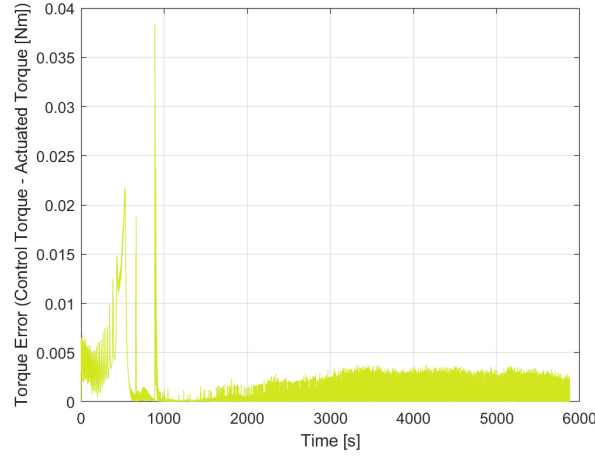
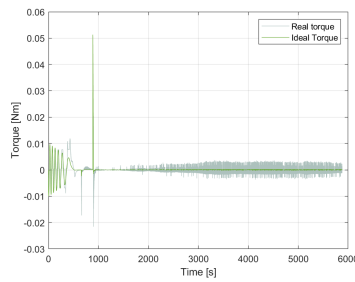
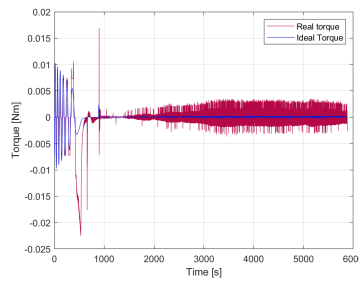


Figure 9.5: Torque error

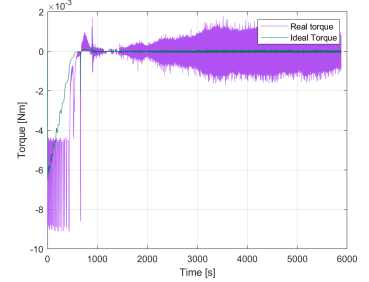
by the datasheet) are consistent with the model. In the tracking phase, however, an "amplified" behaviour is of notice, since the actuators give the spacecraft much more thrust (and torque) than needed, hence the higher than expected error in the second half of the plot in Figure 9.5. This might be due to a white noise value which passing through a low-pass filter results too high considered the very small thrust and torques at hand, but also to a not-perfect tuning of the control torque with the actuators or the limits of our control technique. Moreover, the management of such small torques required, along with a delay imposed, proved difficult without exploiting more filtering. The comparison between components is illustrated in Figure 9.6.



(a) Real vs Ideal Torque (x-component)



(b) Real vs Ideal Torque (y-component)



(c) Real vs Ideal Torque (z-component)

Figure 9.6: Torque components

## 9.5 Statistical Performance Analysis - Monte Carlo

### 9.5.1 Simulation Introduction

After analyzing the results of a specific simulation run, we decided to focus on a sensitivity analysis related to the initial conditions. The aim is to vary the initial state of attitude and angular velocity and observe the behavior of the main parameters of the simulation. This enables us to directly assess the value of certain variables previously defined as negligible, thereby validating these assumptions. The chosen method to perform this analysis is the statistical Monte Carlo approach, which estimates the expected value of a given variable through a stochastic process by randomly varying the parameters governing the phenomenon under investigation.

To apply this method, we first define all the quantities of interest and the Monte Carlo parameters for the simulation.

- Time Required for Maneuvers,  $t_{dt}$ ,  $t_{sw}$
- Mean Disturbance Torques Magnitude,  $M_{GG}$ ,  $M_{SRP}$ ,  $M_{Drag}$ ,  $M_{Mag}$
- Mean Attitude Determination and Pointing Error Euler Angle,  $\theta_{Err}^{Att}$ ,  $\theta_{Err}^{Point}$ ,  $\omega_{Err}$
- Actuator Torque Error and Final Mass,  $T_{Err}$ ,  $m_f$

N Simulations	Attitude Initial Condition	Angular Velocity Initial Condition
100	Uniform Random Unit Quaternion	Uniform Random Velocity $\in \begin{bmatrix} -1 \\ -1 \\ -1 \end{bmatrix} ; \begin{bmatrix} 1 \\ 1 \\ 1 \end{bmatrix} \text{ rad/s}$

Table 9.1: Monte Carlo Analysis Parameters

### 9.5.2 Results Analysis

The results obtained for each simulation are compared to highlight potential statistical distribution relationships and to estimate the expected value and associated uncertainties. Below, graphical and numerical analysis are presented for each main category of quantities under investigation. The graphical analysis is presented with a histogram to highlight the occurrences, supported by a **Kernel Density Estimation**<sup>1</sup>, the **mean value**, and the uncertainty bounds  $\sigma$  e  $2\sigma$ .

#### Maneuver Times

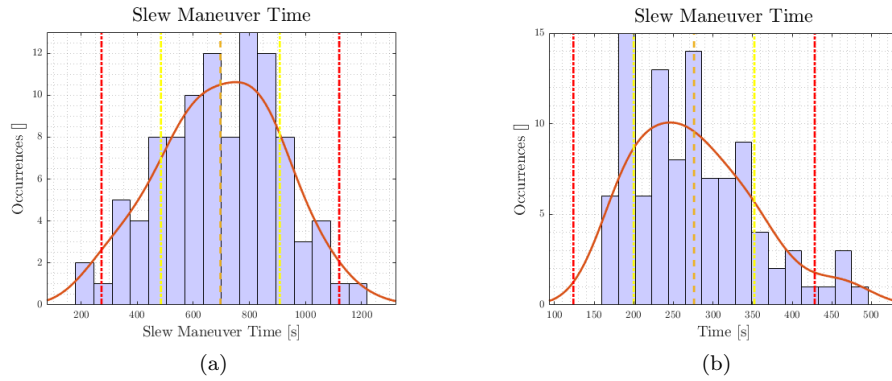


Figure 9.7: Maneuver Times Monte Carlo

Upon analyzing the estimated distribution of maneuver times in the context of theoretical foundations, several observations can be made. First, the duration of the De-Tumbling maneuver exhibits a shape that can be traced back to a normal distribution, slightly skewed toward times greater than the mean. This is likely due to the logic of proportional control with maximum saturation.

Indeed, for higher speeds, the response will also be more aggressive, making the ideal outcome constant and thus the true distribution normal. This condition is met if the maximum expressible torque limit is not exceeded. In this case, saturation leads to a loss of time, which subsequently results in a loss of symmetry.

The slew maneuver distribution, on the other hand, is less evident and is characterized by its high degree of unpredictability. This is due to the substantial torque requirements in the initial stages of maneuvering, which lead to an almost inevitable overshoot of saturation and subsequent asymmetry.

Looking at the numerical values instead, we find that the De-Tumbling maneuver is very likely to take less than one-sixth of the orbit, while the Slew is much shorter, lasting half the time of the first maneuver. Finally we can be happy about the swiftness of our maneuvers.

Parameter	Mean [s]	$\sigma$ [s]	$2\sigma$ [s]
De-Tumbling	696.45	$\pm 212.15$	$\pm 424.30$
Slew	270.06	$\pm 76.12$	$\pm 152.25$

Table 9.2: Statistics Maneuvers

<sup>1</sup><https://it.mathworks.com/help/stats/kernel-distribution.html>

## Disturbance Torques

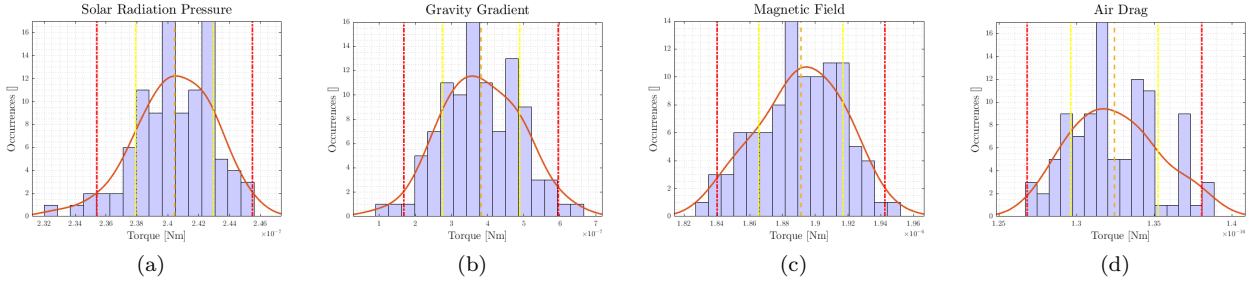


Figure 9.8: Disturbance Torques Monte Carlo

Essentially, if we examine the distribution of the mean magnitude of disturbances across various simulations, we observe an approximately normal trend. Indeed, each disturbance is largely influenced by the pointing phase, the longest phase, which, by exhibiting conditions independent of the initial state, results in constant torques from one simulation to another. Consequently, numerical differences can only arise from the varying conditions in the other flight phases and the time associated with them. Notably, we observe that the assumption of neglecting aerodynamic drag compared to other disturbances is justified. Also, we notice how aerodynamic drag deviates the most in terms of distribution; that's primarily because of the large influence of the uniform random initial rotational velocity conditions, as the primary aerodynamic drag effects manifest during this phase. Finally, we observe that this statistical model is capable of predicting the expected value of at least three out of the four disturbances with remarkable precision. Specifically, the standard deviation in these cases is at least two orders of magnitude smaller, underscoring the model's high level of accuracy.

Parameter	Mean [Nm]	$\sigma$ [Nm]	$2\sigma$ [Nm]
Gravity Gradient	3.822e-7	$\pm 1.0690\text{e-}7$	$\pm 2.137\text{e-}7$
Solar Rad. Pres.	2.404e-7	$\pm 2.520\text{e-}9$	$\pm 5.039\text{e-}9$
Magnetic Field	1.891e-6	$\pm 2.559\text{e-}8$	$\pm 5.117\text{e-}8$
Air Drag	1.324e-16	$\pm 2.814\text{e-}18$	$\pm 5.628\text{e-}18$

Table 9.3: Statistics Disturbances

## Attitude, Velocity and Pointing Errors

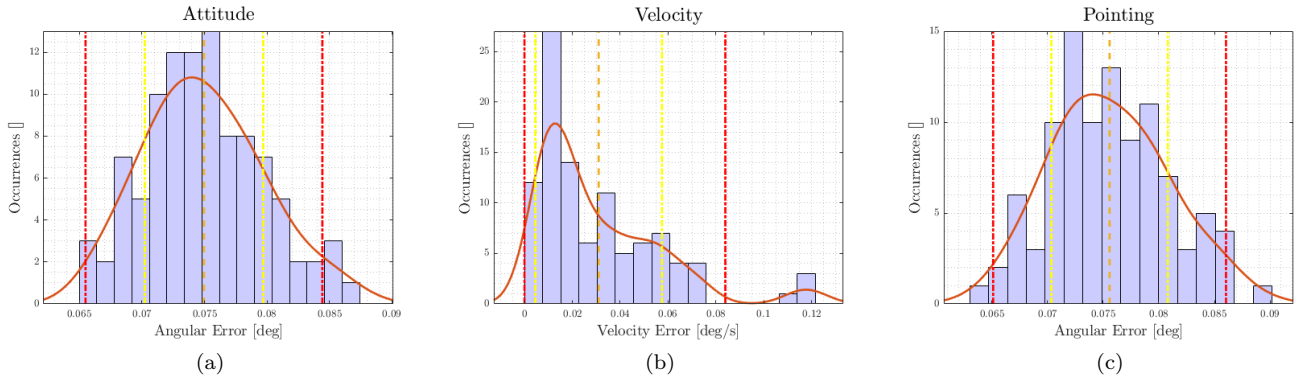


Figure 9.9: Attitude, Velocity and Pointing Errors Monte Carlo

When examining the error parameters for angles, whether related to attitude determination or nadir pointing, we observe a distribution closely resembling a normal distribution, characterized by a low standard deviation—an order of magnitude smaller than the mean. The pointing error is computed exclusively from the end of the slew maneuver and serves as a reliable metric for demonstrating compliance with mission requirements. It is evident that the error associated with attitude determination directly influences the pointing error, as it propagates through the control logic during its computation. This relationship is reflected in the comparable order of magnitude of these errors, with the pointing error consistently remaining smaller.

A different behavior is observed for the error distribution in velocity estimation. This distribution exhibits a distinct asymmetry, driven by the logical constraint of zero error. Specifically, the mode occurs near zero error and gradually decreases beyond that point. While this introduces a higher degree of uncertainty in the measurement, this remains low overall, owing to the instrument's high-performance characteristics.

Parameter	Mean	$\sigma$	$2\sigma$
Attitude	$7.496e-2^\circ$	$\pm 4.733e-3^\circ$	$\pm 9.465e-3^\circ$
Velocity	$3.103e-2^\circ/\text{s}$	$\pm 2.646e-2^\circ/\text{s}$	$\begin{bmatrix} -3.103e-2 \\ +5.291e-2 \end{bmatrix}^\circ/\text{s}$
Pointing	$7.558e-2^\circ$	$\pm 5.230e-3^\circ$	$\pm 1.046e-2^\circ$

Table 9.4: Statistics Attitude, Velocity and Pointing Errors

### Actuator Torque Error and Final Mass

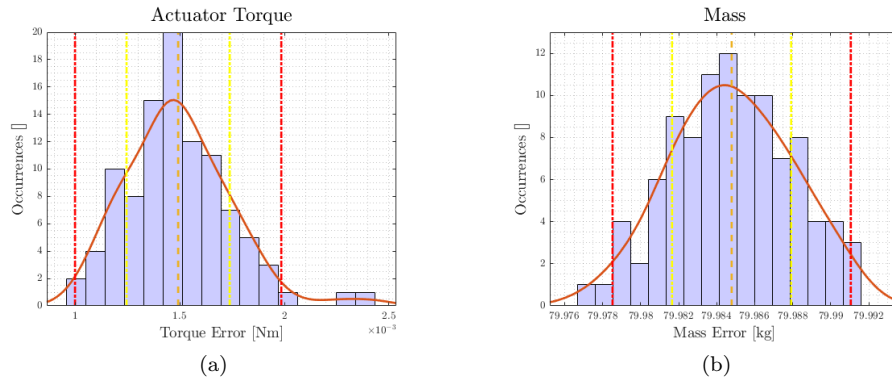


Figure 9.10: Actuator Torque Error and Mass Monte Carlo

Finally, we analyze the variables directly dependent on the actuators, such as the final mass (influenced by the fuel consumed by the actuators) and the torque error. For the latter, we observe that its distribution closely resembles a triangular distribution rather than a normal one, except for an isolated cluster of occurrences at higher values. This anomaly may be linked to simulations where saturation phenomena are more prevalent, leading to a significant increase in the error. Nonetheless, the expected value demonstrates good precision, with the standard deviation being an order of magnitude smaller than the mean. Regarding the final mass, our assumption in the control algorithms to treat it as constant is validated, as the variation is on the order of 15 grams. From a distribution perspective, the final mass also exhibits a normal distribution, with a standard deviation relative to the calculated mean on the order of a few grams, confirming its accuracy with high precision.

Parameter	Mean	$\sigma$	$2\sigma$
Torque Error	$1.492e-3 \text{ Nm}$	$\pm 2.466e-4 \text{ Nm}$	$\pm 4.931e-4 \text{ Nm}$
Mass	$79.9848 \text{ Kg}$	$\pm 3.132e-3 \text{ Kg}$	$\pm 6.263e-3 \text{ Kg}$

Table 9.5: Statistics Torque Error and Final Mass

### 9.5.3 Conclusion

By comparing our metrics with the mission requirements, we can confidently confirm that, for the simulations analyzed, all scenarios are executed successfully, achieving performance levels that exceed the specified requirements.

# References

- [1] Canon Electronics Inc. *CE-SAT-IE specifications*. 2024. URL: <https://en.canon-elec.co.jp/news/successful-launch-and-communication-establishment-of-ce-sat-ie/#post>.
- [2] Franco Bernelli. *Lecture Notes for Spacecraft Attitude Dynamics course*.
- [3] IV Benjamin B. Spratling and Daniele Mortari. *A Survey on Star Identification Algorithms*. Tech. rep. Aerospace Engineering, Texas AM University, College Station, 77843-3141 TX, USA, 2009.
- [4] Jena-Optronik GmbH. *Jena-Optronik ASTRO APS datasheet*.
- [5] Gran Stal Solutions Ltd. *GS-FOG70A datasheet*.